MDPI

Article

Controlling Factors of Meteoric Diagenesis in Karst Reservoirs: An Example from the Majiagou Formation, Ordos Basin, China

Jiaqi Yang [1,2,3], Juntao Zhang [2], Zhiliang He [4,*], Macro Brandano [3,*] and Chongyang Wu [2]

1. School of Energy Resources, China University of Geosciences, Beijing 100083, China; yangjiaqi323@163.com
2. Key Laboratory of Deep Geology and Resources, SINOPEC, Beijing 100083, China
3. Dipartimento di Scienze della Terra, Sapienza Università di Roma, P.le Aldo Moro 5, 00185 Roma, Italy
4. China Petrochemical Corporation Ltd., Beijing 100728, China
* Correspondence: hezhiliang@cugb.edu.cn (Z.H.); marco.brandano@uniroma1.it (M.B.)

Abstract: Karst reservoirs have always been a key field of oil and gas exploration. However, quantifying the process of meteoric transformation remains a persistent challenge that limits the accuracy of reservoir quality prediction. To explore the controlling factors of meteoric cementation on karst reservoirs, the Majiagou Formation of the Ordos Basin in China was selected as an example. The petrology; carbon, oxygen, and strontium isotopes; and in situ major, trace, and rare earth elements were used, types and origins of calcite cements were analyzed in detail. The results revealed five types of calcite cements (Cal-1~Cal-5), four types of cathodoluminescence (CL) intensities (dull, dull red, deep red, and bright red luminescence), and six types of rare earth element patterns (Pattern-1~Pattern-6). These five types of calcite cements developed in three periods. Cal-1 (transition CL) and Cal-2 (dull CL) were precipitated during the Early Pennsylvanian period, the meteoric freshwater was clean; Cal-3 (transition CL) and Cal-4 (bright red CL) were precipitated at the end of the Late Carboniferous period, the fluids had strong dissolution ability and were polluted by terrigenous debris; Cal-5 (transition CL) was deposited during the burial period, the fluid was pure pore water or groundwater. The control of the cement on the reservoir during the burial period was much weaker than that of meteoric cements. Therefore, explorations of karst reservoirs should be focused on weak cementation during the epigenetic period.

Keywords: meteoric cementation; in situ elements; cathodoluminescence; rare earth elements; Majiagou Formation; Ordos Basin

1. Introduction

Karst reservoirs are a significant focus for oil and gas exploration all over the world, and different degrees of karst transformation in carbonate reservoirs have been discovered [1]. The formation mechanism and transformation process of high-quality karst reservoirs are critical scientific problems of scholarly concern [2,3]. Exploring variables that control meteoric dissolution and cementation difference in karst reservoirs will be conducive to attaining a more comprehensive and profound understanding of these scientific problems.

Statistics indicate that the reservoirs of 20% to 30% of large gas fields are carbonate karst reservoirs related to regional unconformity [4]. Interest has increased in studying karst patterns, such as those in the layered carbonates in the Salitre Formation, São Francisco Craton, Brazil [5–7], and their association with Brazilian presalt carbonate reservoirs [8], as well as those from the Paleogene in the southwest of the Zagros Basin [9]. Moreover, karst reservoirs are a key reservoir type in the marine petroliferous basins of China. There are large gas fields related to karst reservoirs that developed in the Ordos Basin during the Middle Ordovician, in the Tarim Basin during the middle-late Cambrian and late Ordovician, and in the Sichuan Basin during the Precambrian and the Carboniferous [10–13]. Key characteristics of these carbonate karst reservoirs are long development time, multiple karst periods, and complex reservoir evolution, all of which make them difficult to explore [14].

Majiagou Formation (Majiagou Fm.) carbonate reservoirs have their own unique attributes, because they are composed of evaporites and carbonate rock assemblages under the influence of paleogeographical location and paleoclimate [15]. There are large-scale micrite dolomite reservoirs containing irregular-circular gypsum mold pores that are rarely found elsewhere [16–18]; these gypsum mold pores are filled with calcite cement or residual gypsum minerals [19–21]. These coarse-grained secondary calcites originated from meteoric freshwater during epigenetic diagenesis [13,22]. Therefore, to explore the evolution law of Majiagou Fm. reservoirs, it is essential to analyze the meteoric diagenetic process.

The influence of meteoric diagenesis on karst reservoirs mainly includes the development of dissolution pores, vugs, and fractures, or the precipitation of meteoric cements. The geochemical characteristics of carbonate sediments contain rich geological information [23,24]; however, different minerals and types of cements are difficult to obtain and distinguish by bulk geochemical methods. Notably, the rise of in situ elemental experiments provides a means to explore the types and precipitation environments of meteoric calcite [25]. Meteoric cement is a high-quality proxy of restored paleoenvironmental and paleoclimatic conditions in carbonate-dominated strata [26–28], because it equilibrates slowly at average annual temperatures and is unaffected by biological effects that might bias other proxy materials [29]. The potential of in situ trace element solutions in carbonate minerals to reconstruct environmental characteristics in low-temperature (marine or diagenetic) environments has attracted extensive attention [30,31]. Paleoredox conditions can be inferred in part from the contents of iron and magnesium [28,32]. The characterization of in situ rare earth elements (REE) enabled the origin of the Ordovician hydrothermal dolomite in the Tazhong Uplift, China to be resolved [33].

The origin of the coarse-grained calcite precipitated in the Majiagou Fm. Ordos Basin is only thought to be freshwater precipitation based on petrological characteristics and on analysis of powder isotopes and elements; however, potential differences in environment and fluid source have not been explored further. In a recent study, in situ U-Pb dating technology was used to determine that the meteoric calcites are multiphase cementation formed at 319.0~292.7 Ma in the study area [22]. In the present study, cementations in the Middle Ordovician Majiagou Fm. carbonate reservoir in the Ordos Basin were analyzed in detail, using cathodoluminescence (CL) characteristics and in situ elemental analysis methods, combined with data for powder carbon, oxygen, and strontium isotopes. The characteristics of cementation during the epigenetic period were further divided, and the sources of different types of cement in the gypsum mold pores and associated fractures were systematically distinguished. The findings provide a reference for the transformation process and formation mechanism of karst reservoirs and guided natural gas exploration.

2. Geological Setting

The Ordos Basin is located in the western part of the North China Craton (NCC), with an area of approximately 25×10^4 km^2 (Figure 1a), and it can be divided into six structural units: the Yimeng Uplift, the Weibei Uplift, the Jinxi Fault–Fold Belt, the Yishan Slope, the Tianhuan Syncline, and the Fault–Fold Belt of the Western Margin (Figure 1b). The Ordos Basin was near the equator during the Middle Ordovician, affected by high temperatures, a large number of gypsum rocks were co-deposited with carbonate rocks during regression (Figure 1c). There are three transgressions (second, fourth, and sixth members of the Majiagou Fm., Ma2, Ma4, and Ma6) and three regressions (Ma1, Ma3, and Ma5) in the Majiagou Fm. Ma1, Ma3, and Ma5 mainly developed sulfate and carbonate rock assemblages; the Ma2 and Ma4 members are mainly carbonated rocks, and only some parts of the basin still have the remaining Ma6, which is dominated by carbonate rocks [15]. The Majiagou Formation comprises carbonate rocks deposited in the main part of the Ordos Basin and generally has deposits that are several hundred meters thick.
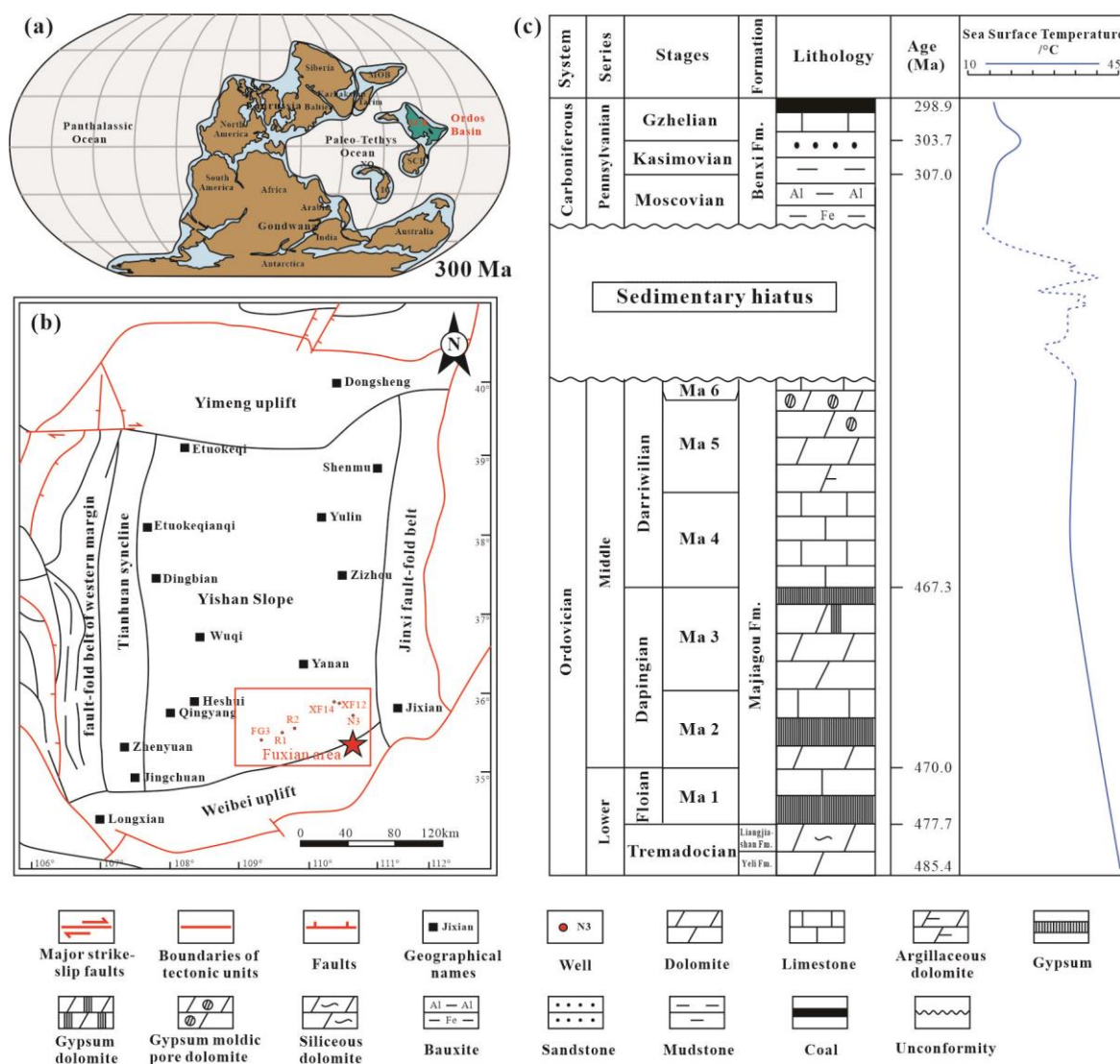
Figure 1. (**a**) Paleogeographic reconstructions of the Ordos Basin at 300 Ma. IC, MOB, NCB, NQ, Qm, and SCB indicate the Indochina, Mongolian, North China, North Qiangtang, Qaidam, and South China blocks/terranes, respectively, modified from ref. [34]; (**b**) map showing the location of Fuxian area in the Ordos Basin, and the specific core wells locations; (**c**) stratigraphic, lithology and paleotemperature characteristics from Ordovician to Carboniferous in the study area, sea surface temperature modified from ref. [35].

Affected by the Caledonian movement, the basin was uplifted in the Late Ordovician, and experienced weathering up to 130 Ma; Late Ordovician to Early Carboniferous strata are missing (Figure 1c) [36]. Until the end of the Hercynian movement, under the compression of the North and South troughs, seawater gradually withdrew from the basin area, forming a craton basin that was steep in the south and gentle in the north [37,38].

Carbonate platform with low terrain and uplifted periphery were in the basin from Ma1 to Ma3, but the paleogeomorphology of Ma4 to Ma6 varied greatly because it was affected by the high-frequency variation of the sea level [39,40]. The present study focused on Ma5, which corresponds to the Dapingian–Darriwilian and was mostly deposited in a limited tidal flat environment. Under the influence of high-salinity seawater, the dolomite strata often contain gypsum-salt rocks and/or layers [41].

The Ordovician was an important geological period for the tectonic climate and biological evolution of the early Paleozoic. In addition, the Late Paleozoic Ice Age (LPIA), which lasted approximately 100 Ma (*ca*. 360–255 Ma), is a critical turning point in global

climate change [42,43]. However, the LPIA was not a long-term continuous glaciation but rather an overall cold glacial event separated by multiple warm events [44]. The precipitation of calcite cement may be the result of multiple warm events in the study area during the Late Carboniferous [45–47].

3. Samples and Methods

3.1. Samples Selected

We investigated the Ma5 member dolomite from some drilling wells (R1, R2, FG3, XF2, XF14, and N3) in remnants, Fuxian area, Ordos Basin (Figure 1b). Cores of these drilling wells included Majiagou Fm. karst reservoirs. A total of 23 samples were polished as thin sections for petrological, mineralogical and morphological observations. Types and morphology of carbonate minerals were observed by an OLYMPUS BX51 microscope. The CL imaging were performed on polished and carbon-coated samples to characterize the morphology of minerals. The imaging was conducted with a Quanta 450 FEG SEM equipped with a SDD Inca X–Max 50 and a MonoCL 4 + detector (20 kV accelerating voltage and 20 nA beam current) at the Beijing Research Institute of Uranium Geology, China.

Four representative thin sections were selected for in situ major, trace, and rare earth element analysis. Powdered samples were selected for geochemical analyses (e.g., $\delta^{13}C$, $\delta^{18}O$, and $^{87}Sr/^{86}Sr$), using a micro-mill with a drilling bit diameter of 0.25 mm. To distinguish between matrix and cement, a total of 20 samples were collected for C and O isotope analysis, and 16 samples were collected for Sr isotope analysis.

3.2. In Situ Elemental Analysis

Concentrations of 57 major, trace, and rare earth elements were determined by performing in situ elemental analysis under room temperature in the Research Branch of Southwest Petroleum University, Key Laboratory of Carbonate Reservoirs, China National Petroleum Corporation (CNPC). The test sample was a special sheet prepared for the laser ablation inductively coupled plasma mass spectrometry (LA-ICP-MS) experiment (thickness 0.04 mm, size 17 mm × 25 mm). Before the test, ultrasonic waves were applied to the sample for 90 min to remove surface impurities; then, the sample was air-dried in a fume hood. The test instrument was a Newwave 193 nm UC laser connected to an Agilent 7800 ICP-MS mass spectrometer; the laser beam spot was 80 microns in diameter, and the frequency was 10 Hz. The standard sample was USGS MACS-3 (calcium carbonate; United States Geological Survey), the monitoring standard sample is JCp-1. To calibrate and calculate the measurement results, a series of reference materials were analyzed before and after the analytical batch and were also inserted within the sequence every five sample positions to ensure the error was less than 10%.

We normalized the REE data with Post-Archean Australian Shale (PAAS) standard samples. Because the Eu of PAAS has a negative anomaly, a chondrite standard sample was selected to normalize the data to avoid incorrectly evaluating the δEu, and the specific calculation formula can be found in ref. [48]. The concavity index (*CI*) refers to the concavity of the PAAS-normalized REE patterns, and a *CI* value of ~1 indicates a quasi-linear shale-normalized partitioning pattern. The following equation was used to calculate the *CI*:

$$CI = Gd_{SN}/(La^6{}_{SN} \times Yb^7{}_{SN})^{1/13}$$

3.3. Bulk C, O, and Sr Isotopes

Approximately 10 mg of the rock powder samples was reacted with pure phosphoric acid at 72 °C for 1 h. The released CO_2 was collected and tested for C and O isotope composition in a Mat 253 Mass Spectrometer. The results were calibrated and expressed as Vienna Pee Dee Belemnite VPDB (‰); the accuracy was better than ±0.2‰. For strontium isotopes analysis, ~100 mg powder was reacted in a Finnigan Mat Triton Tl with 6 M HCl for 24 h at 100 °C. The tested $^{87}Sr/^{86}Sr$ ratios were calibrated with a standard from the

National Institute of Standards and technology (NBS-987), which has an $^{87}Sr/^{86}Sr$ ratio of 0.710273 ± 0.000012.

4. Results

4.1. Petrological Characteristics

The Majiagou Fm. mainly developed microcrystalline dolomite reservoirs, the matrix was dolomite with a particle size of ~5 μm, and the cements were mostly developed in the gypsum mold pores and associated fractures (Figure 2). The cement mainly consisted of coarse-crystalline calcite, usually larger than 500 μm. Dolomite silt (Dol-1) was observed in pores and fractures (Figure 2a). Calcite- and dolomite-embayed contacts formed by dedolomitization which were common in the matrix (Figure 2b). Various types of calcite cements were observed under CL; the CL intensities were dull, dull red, deep red, and bright red luminescent (Figure 2c–h). Five types of calcite cements were present in the study area; dull red ring-shaped calcite cements with complete crystal structure, mainly developed at the edges of the gypsum mold pores (Cal-1) (Figure 2c,d); dull luminescent calcite cement mainly developed within the cores with earlier precipitation (Cal-2) (Figure 2d,e); bright red cement, mainly developed in the gypsum mold pores (Cal-4) (Figure 2f); and widely distributed dull red and deep red calcite cement (Cal-3) developed at the transition position between Cal-2 and Cal-4 (Figure 2e). The fluid inclusions indicated that there was a type of calcite cement formed during the burial period (Cal-5) (Figure 2g–i). The CL intensity of Cal-5 was between dull red and deep red luminescent, and the homogeneous temperature was >100 °C (Table 1).
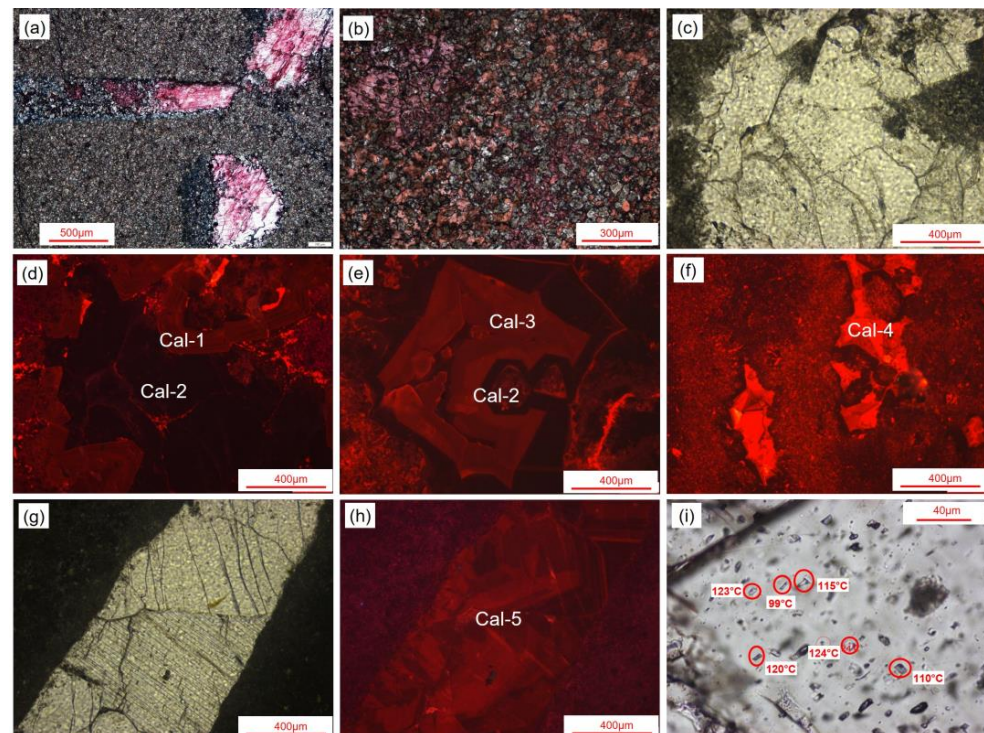

Figure 2. Characteristics of reservoirs in Majiagou Formation, Ordos Basin ((**a**) N3-1, Ma_5^1 submember, gypsum mold pores filled with dolomite silt and calcite cement; (**b**) R2-21-2, Ma_5^1 submember, dolomite and calcite embayed contacts formed by dedolomitization; (**c**,**d**) XF14-2, Ma_5^2 submember, the euhedral Cal-1 precipitated at the edge of the gypsum mold pore, and the dull luminescent Cal-1 precipitated subsequently; (**e**) N3-17, Ma_5^{1+2} submember, Cal-2 was precipitated in crack associate with gypsum mold pore; (**f**) N3-16, Ma51 submember, Cal-4 precipitated inner the mold pore; (**g**,**h**) XF14-10B, Ma_5^2 submember, Cal-5 precipitated in the crack associated with the gypsum mold pores, and the CL intensity is alternating dull red and deep red c; (**i**) XF14-10B, $Mfva_5^2$ submember, fluid inclusions in Cal-5).

Table 1. Statistics of fluid inclusion microthermometry for meteoric calcites from the Majiagou Formation, Ordos Basin.

Lithofacies	Morphology		Th (°C)	Tm (°C)	Salinity (wt% NaCl)	
Gypsum mold pore	Strip, Quadrilateral, Triangle, Circle	Mean	115	−20	22.3	n = 6
		Max	124	−19	23.0	
		Min	99	−21	21.7	
Crack	Strip, Quadrilateral, Oval	Mean	111	−20	22.5	n = 6
		Max	123	−19	23	
		Min	96	−21	21.7	

4.2. In Situ Elemental Characteristics

The in situ experiments showed that the major and trace elements of the calcite cements varied greatly. Major elements included Al, Fe, and Mn. The Al contents in Cal-1~Cal-5 were 0.28–91 ppm, 0.21–1092 ppm, 0.02–15.4 ppm, 0.23–6 ppm, and 0.07–103 ppm, respectively; the Fe contents were 1244–1860 ppm, 752–4420 ppm, 788–3800 ppm, 767–2190 ppm, and 894–972 ppm, respectively; the Mn contents were 4.9–205 ppm, 0.09–980 ppm, 15–1250 ppm, 0.4–3250 ppm, and 24.4–75.9 ppm, respectively. Regarding the trace elements, the contents of Sr were 13.7–76.8 ppm, 4.79–326 ppm, 31.5–788 ppm, 11.86–520 ppm, and 95.7–367 ppm, respectively; those of Ba were 0.06–0.99 ppm, 0.02–4.04 ppm, 0.12–1.88 ppm, 0.04–1.83 ppm, and 0.04–0.68 ppm, respectively (Table 2). For the specific location of and data for the in situ experiment, please refer to Figure S1.

The $\sum$REE was 0.6–726.9 ppm, with an average of 135.6 ppm; δCe_{SN} was 0.03–4.65, and the δCe_{SN} values of Cal-1~Cal-5 were 0.77–2.55, 0.03–2.73, 0.04–4.51, 0.13–2.53, and 0.90–1.22, respectively; δEu_{CN} was 0.53–0.81. The $(La/Yb)_{SN}$ ranged from 0.08 to 9.27. The $\sum$REE of Cal-1 was low: all values were distributed around 10 ppm, and only one location exceeded 30 ppm; the $\sum$REE of Cal-2 was 0.61–164.85 ppm; the $\sum$REE of Cal-3 was 17.30–637.24 ppm; the $\sum$REE of Cal-4 was 7.87–726.95 ppm, which was the highest among all the cements; the $\sum$REE of Cal-5 was 1.53–32.29 ppm. The CIs of Cal-1~Cal-5 were 1.53–3.56, 1.16–6.49, 1.53–7.28, 2.44–5.83, and 0.96–1.85, respectively.

There were differences in the contents and the distribution patterns of REE in the matrix and in the cement. PAAS standards were used to standardize the obtained REE, and the distributions revealed six patterns (Pattern-1~Pattern-6). Pattern-1 was a flat type (Figure 3a); Pattern-2 was a positive Ce anomaly (Figure 3b); Pattern-3 was a negative Ce anomaly (Figure 3c); Pattern-4 was mid-REE (MREE) enriched (Figure 3d); Pattern-5 was heavy-REE (HREE) depleted and monotonically decreasing (Figure 3e); Pattern-6 was positive La and Gd anomalies (Figure 3f). The patterns of the matrix were Pattern-1 and Pattern-2, those of the calcite cements were Pattern-1~Pattern-5, and that of the dolomite silt was Pattern-6.

Table 2. In situ elemental characteristic of Majiagou Formation, Ordos Basin.

Location	Type	Al	Mn	Fe	Sr	Ba	La	Ce	Pr	Nd	Sm	Eu	Gd	Tb	Dy	Ho	Er	Tm	Yb	Lu
XF14-2-5		0.3	205.0	1860	13.7	/	1.72	5.00	0.75	3.02	1.07	0.19	1.07	0.14	0.71	0.13	0.37	0.05	0.28	0.05
XF14-2-7	Cal-1	21.3	124.1	1391	34.2	0.06	0.80	1.87	0.25	1.16	0.42	0.09	0.59	0.08	0.46	0.08	0.21	0.03	0.16	0.03
XF14-2-8		91.0	59.6	1381	76.8	0.66	9.30	21.9	0.93	3.48	0.75	0.17	0.65	0.07	0.34	0.05	0.13	0.02	0.11	0.02
XF14-2-9		2.4	62.8	1450	73.1	0.99	0.88	2.72	0.30	1.28	0.36	0.07	0.33	0.05	0.23	0.04	0.10	0.02	0.07	0.01
N3-16-5		80.0	898.0	2410	326.0	1.35	18.10	57.3	8.26	40.60	11.28	2.37	10.60	1.45	7.49	1.29	3.09	0.37	2.32	0.33
N3-16-6		1092.0	980.0	2440	192.0	4.04	10.80	34.00	4.74	21.90	5.85	1.22	5.52	0.77	4.20	0.74	1.81	0.22	1.35	0.20
N3-16-9		0.43	1.0	1630	11.5	/	1.77	0.35	1.53	8.05	2.31	0.46	2.59	0.37	2.43	0.48	1.28	0.16	0.89	0.13
N3-16-10		0.6	28	1580	14.9	0.17	0.175	0.86	0.09	0.44	0.11	0.02	0.10	0.02	0.12	0.02	0.08	0.01	0.08	0.01
N3-17-1		3.9	13.1	911	20.9	0.10	1.74	1.70	0.72	3.04	0.68	0.12	0.71	0.10	0.59	0.12	0.31	0.04	0.25	0.04
N3-17-12	Cal-2	0.3	26.0	761	5.7	0.02	5.10	0.39	1.84	8.40	1.63	0.33	2.02	0.26	1.63	0.35	0.88	0.10	0.55	0.08
N3-17-15		0.8	3.5	752	10.7	0.28	3.63	0.62	1.71	8.17	1.69	0.32	1.66	0.21	1.25	0.28	0.72	0.09	0.53	0.08
N3-17-18		0.4	369.0	4420	235.0	0.16	0.63	0.86	0.09	0.87	0.96	0.28	1.55	0.19	1.02	0.18	0.44	0.06	0.38	0.05
XF14-2-6		0.2	0.1	1169	5.5	0.66	0.154	0.03	0.07	0.40	0.14	0.03	0.19	0.03	0.18	0.04	0.11	0.02	0.11	0.02
XF14-2-12		1.1	/	1152	4.8	0.59	0.80	0.53	0.70	3.51	1.44	0.24	1.46	0.20	1.00	0.16	0.39	0.05	0.28	0.04
XF14-2-13		/	/	1079	11.9	0.54	0.35	0.02	0.01	0.07	0.03	0.01	0.04	0.01	0.03	0.01	0.01	0.00	0.01	0.00
N3-16-3		1.3	547.0	2000	520.0	0.76	26.10	82.00	13.1	65.30	19.90	4.38	21.40	3.28	18.40	3.37	8.40	1.04	5.96	0.84
N3-16-4		4.0	800.0	2670	367.0	0.49	10.50	34.00	4.83	22.50	5.68	1.25	6.41	0.90	4.89	0.85	1.99	0.21	1.18	0.16
N3-16-8		0.2	783.0	1960	31.5	0.32	1.58	10.00	0.60	2.68	0.63	0.11	0.60	0.09	0.47	0.09	0.24	0.03	0.17	0.02
N3-16-13		2.2	1240.0	1530	427.0	1.44	71.50	201.00	28.30	127.00	27.50	5.00	21.60	2.70	13.50	2.34	5.61	0.71	4.24	0.61
N3-16-15		3.6	495.0	1270	412.0	1.78	16.70	53.80	8.50	41.20	12.20	2.59	12.20	1.83	10.00	1.80	4.49	0.54	3.13	0.44
N3-16-16		15.4	760.0	1870	216.0	0.59	7.10	24.10	3.25	14.60	3.58	0.70	3.35	0.44	2.24	0.40	0.90	0.11	0.69	0.10
N3-17-2		/	488.0	3800	192.0	/	3.50	19.90	4.60	29.20	11.10	2.19	9.60	1.30	7.10	1.24	2.93	0.35	2.10	0.31
N3-17-3		0.7	485.0	1880	272.5	1.88	12.15	49.40	8.21	40.50	12.04	2.54	12.30	1.93	10.69	1.86	4.60	0.58	3.74	0.55
N3-17-7		0.1	564.0	797	446.0	0.12	38.30	110.00	15.23	67.10	15.77	3.11	14.80	1.88	9.33	1.53	3.43	0.40	2.40	0.37
N3-17-8	Cal-3	0.4	567.0	827	650.0	0.34	11.29	46.60	7.92	38.50	13.92	3.12	15.39	2.15	11.00	1.82	4.06	0.47	3.01	0.42
N3-17-9		0.2	782.0	788	321.0	0.18	76.00	199.00	25.90	108.00	19.20	3.32	14.60	1.61	7.50	1.20	2.69	0.32	1.90	0.28
N3-17-10		0.4	775.0	835	427.0	0.16	10.10	36.70	5.91	29.60	10.74	2.49	13.20	1.83	9.59	1.61	3.76	0.45	2.97	0.46
N3-17-11		8.0	15.0	819	36.6	0.29	22.99	2.89	8.63	36.80	6.91	1.15	5.57	0.66	3.43	0.62	1.50	0.18	1.04	0.16
N3-17-14		2.4	693.0	1180	215.3	/	97.00	272.00	38.4	171.00	28.5	4.31	15.90	1.28	4.94	0.76	1.67	0.19	1.12	0.17
N3-17-16		0.3	746.0	1490	413.0	1.28	10.20	51.30	9.40	50.70	17.10	3.67	17.30	2.72	14.80	2.46	5.86	0.71	4.43	0.62
N3-17-17		3.3	437.0	3570	210.0	0.44	9.10	59.00	11.20	68.00	21.40	3.83	17.60	2.32	12.40	2.07	5.10	0.62	3.93	0.58
N3-17-19		6.5	490.0	1620	788.0	0.61	18.10	110.00	21.80	123.00	47.20	10.99	52.50	8.21	45.10	7.44	17.0	2.02	12.3	1.66
XF14-2-3		0.0	830.0	1681	34.2	0.43	14.00	95.00	3.43	11.80	2.68	0.48	2.42	0.32	1.77	0.32	0.94	0.13	0.90	0.15
XF14-2-11		/	1250.0	1983	45.7	0.41	13.19	164.00	3.82	13.90	3.38	0.53	2.64	0.33	1.71	0.31	0.86	0.13	0.83	0.14

Table 2. *Cont.*

| Location	Type	Al	Mn	Fe	Sr	Ba	La	Ce	Pr	Nd	Sm	Eu	Gd	Tb	Dy	Ho	Er	Tm	Yb	Lu
N3-16-1		6	439.0	2190	234.0	1.83	15.00	43.80	6.60	31.50	8.50	1.76	8.25	1.19	6.42	1.16	2.88	0.35	2.02	0.29
N3-16-2		0.3	2150.0	2050	390.0	0.15	94.00	244.90	34.50	158.60	29.70	5.29	22.10	2.35	11.03	1.85	4.28	0.48	2.85	0.39
N3-16-12		3	1690.0	1470	520.0	0.04	103.00	279.00	39.40	178.00	38.30	7.41	32.10	4.29	22.10	3.88	9.70	1.23	7.46	1.08
N3-17-4	Cal-4	0.5	1190.0	987	314.0	0.32	0.58	0.94	0.17	1.22	0.69	0.21	1.15	0.21	1.21	0.22	0.57	0.07	0.53	0.09
N3-17-5		1.9	1209.0	1260	359.0	0.45	37.00	86.00	4.93	24.70	7.78	1.72	8.14	1.07	5.32	0.88	1.94	0.24	1.56	0.22
N3-17-13		0.7	702.0	767	90.1	0.17	19.80	65.10	9.48	42.00	8.21	1.47	6.41	0.74	3.42	0.58	1.27	0.13	0.81	0.13
XF14-2-1		0.9	3250.0	1541	112.0	0.17	1.30	8.20	0.41	1.67	0.59	0.10	0.64	0.09	0.54	0.11	0.32	0.04	0.24	0.04
XF14-2-2		0.2	0.4	1208	11.9	0.04	2.49	2.80	2.99	14.30	4.67	0.74	3.52	0.39	1.99	0.35	0.85	0.10	0.66	0.10
XF14-10B-1		/	67.5	972	95.7	/	1.66	2.83	0.32	1.20	0.17	0.03	0.14	0.02	0.10	0.02	0.05	0.01	0.04	0.01
XF14-10B-2		/	38.8	958	199.0	0.04	9.79	14.60	1.46	5.02	0.55	0.09	0.35	0.07	0.17	0.03	0.07	0.01	0.08	0.02
XF14-10B-3		0.3	75.7	920	103.6	/	0.68	1.08	0.11	0.45	0.10	0.02	0.15	0.02	0.12	0.03	0.06	0.01	0.06	0.01
XF14-10B-4	Cal-5	103.0	24.4	922	333.0	0.68	2.79	4.71	0.52	1.92	0.40	0.07	0.35	0.05	0.25	0.05	0.12	0.01	0.07	0.01
XF14-10B-5		4.3	39.8	960	226.0	0.11	1.48	2.93	0.33	1.20	0.26	0.04	0.22	0.03	0.17	0.03	0.08	0.01	0.05	0.01
XF14-10B-6		0.6	75.9	899	111.8	0.09	0.48	0.65	0.06	0.20	0.03	0.01	0.04	0.01	0.02	0.01	0.01	0.00	0.01	0.00
XF14-10B-8		0.8	44.0	908	202.0	0.15	1.58	3.17	0.36	1.385	0.28	0.05	0.21	0.03	0.16	0.03	0.07	0.01	0.06	0.01
XF14-10B-9		1.4	26.4	894	367.0	0.52	3.19	6.01	0.68	2.39	0.46	0.08	0.47	0.05	0.32	0.06	0.16	0.02	0.11	0.02
N3-16-14	Dol-1	1750.0	295.1	5420	91.0	3.78	12.70	22.90	0.69	2.26	0.62	0.14	4.90	0.16	0.40	0.07	0.18	0.02	0.12	0.02
XF14-2-10		1310.0	502.0	3050	28.8	7.40	9.60	15.60	0.80	3.05	0.70	0.16	4.90	0.20	0.77	0.16	0.45	0.06	0.36	0.05
N3-16-7		442.0	880.0	2920	72.0	2.97	5.00	20.00	1.59	7.25	2.15	0.47	2.32	0.34	2.03	0.30	0.98	0.12	0.78	0.11
N3-16-11		518.0	967.0	1850	72.0	2.42	15.30	56.00	1.54	6.82	1.96	0.40	2.06	0.31	1.79	0.34	0.92	0.11	0.75	0.10
N3-17-6	Matrix	741.0	925.0	7980	75.4	2.60	4.90	9.10	0.74	3.87	1.34	0.32	1.53	0.22	1.23	0.23	0.57	0.07	0.40	0.05
XF14-10B-7		609.0	24.5	732	70.4	1.18	1.24	1.68	0.15	0.51	0.11	0.02	0.12	0.02	0.11	0.02	0.07	0.01	0.05	0.01
XF14-2-4		425.0	151.7	3360	41.1	3.39	3.40	8.60	0.60	2.23	0.63	0.11	0.60	0.07	0.40	0.07	0.17	0.02	0.13	0.02
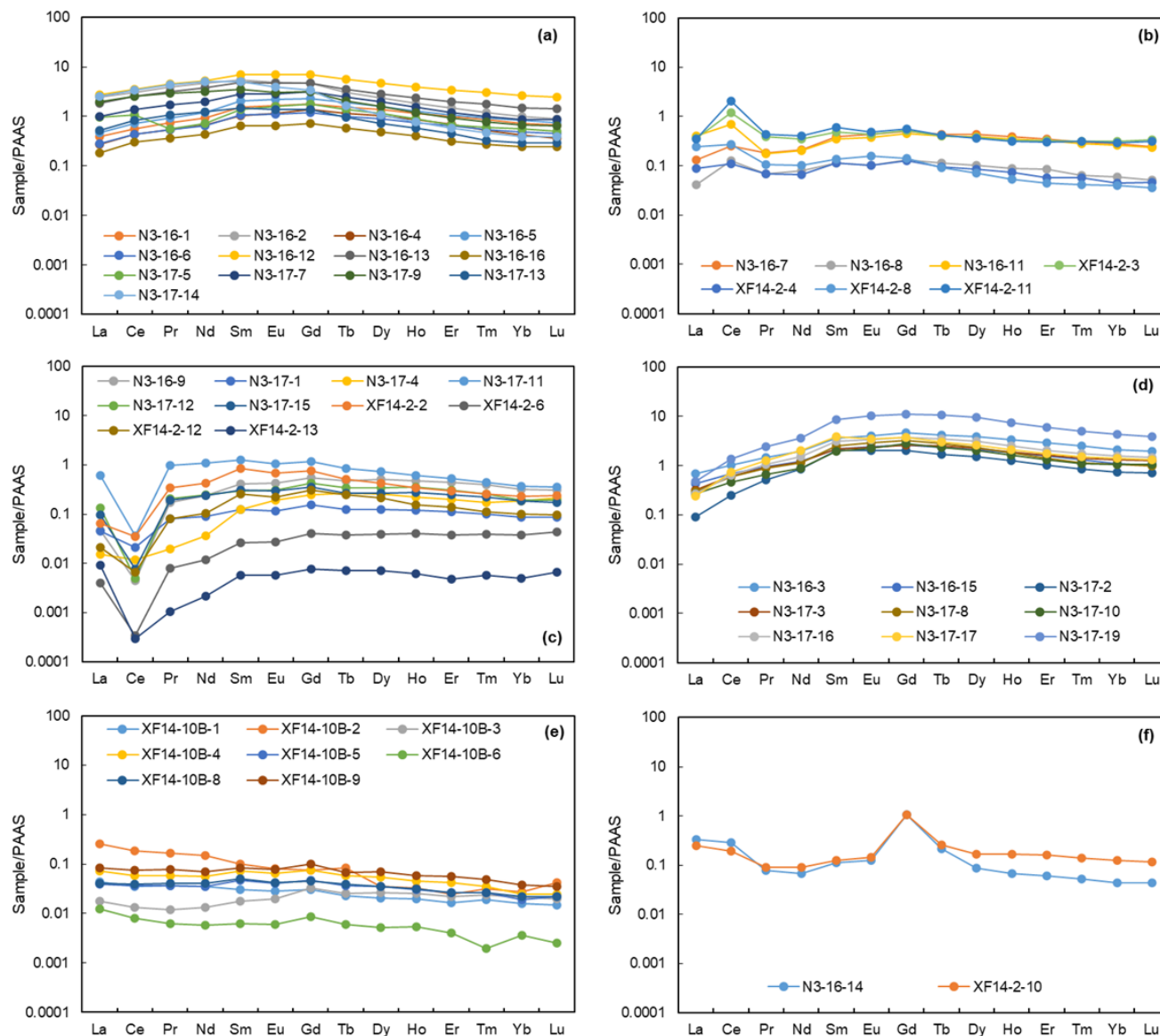
Figure 3. REE distributions of matrix and cement in Majiagou Formation, Ordos Basin ((**a**,**b**) REE Pattern-1 and Pattern-2 of matrix; (**a**–**e**) REE Pattern-1~Pattern-5, which come from Cal-1~Cal-5; (**f**) REE Pattern-6 of Dol-1).

4.3. Isotopic Characteristics

C and O isotopes showed variations in different lithologic samples (Table 3). Except for one sample (N3-11, −5.2‰), the $\delta^{13}C$ contents of the matrix were concentrated in −2.8‰~+0.2‰, with an average of −1.0‰; and the $\delta^{18}O$ contents were −9.8‰~−5.2‰, with an average of −7.1‰ (the $\delta^{18}O$ content of N3-11 was −8.3‰). The $\delta^{13}C$ and $\delta^{18}O$ contents of calcite cement were −10.9‰~−2.6‰ (average −6.3‰) and −14.5‰~−9.2‰ (average −12.0‰), respectively (Figure 4). However, the characteristics of Sr isotope were different from C and O isotopes. The $^{87}Sr/^{86}Sr$ ratio of the matrix and cement were similar (Table 3), ranging from 0.708567 to 0.710641 (average, 0.709576) and 0.708928 to 0.712807 (average, 0.710468), respectively (Figure 5).

Table 3. Characteristics of C/O, and Sr isotopic compositions of Majiagou Formation, Ordos Basin.

Sample	Depth, m	Type	C/O Isotopic Compositions, ‰			Sr isotopic Compositions	
			$\delta^{13}C_{V-PDB}$	$\delta^{18}O_{V-PDB}$	$\delta^{18}O_{V-SMOW}$	$^{87}Sr/^{86}Sr$	S.D.
N3-11	2967.34	Matrix	−5.2	−8.3	22.3	0.708859	0.000015
		Calcite cement	−8.7	−13.7	16.8	0.708928	0.000019
R1-21-3	2997.45	Matrix	−2.8	−9.8	20.8	0.708567	0.000015
		Calcite cement	−7.1	−14.5	16	0.709384	0.000018
R1-21-8	2987.7	Matrix	−0.9	−6.7	24	/	/
		Calcite cement	−5.9	−9.2	21.4	/	/
R1-21-10	2987.55	Matrix	−1.8	−8.2	22.4	/	/
		Calcite cement	−5.7	−10.4	20.2	/	/
R1-21-13	2987.38	Matrix	−0.9	−8.3	22.4	/	/
		Calcite cement	−4	−13	17.5	/	/
R2-21-3	3092.5	Matrix	−0.6	−6.4	24.3	0.709917	0.000013
		Calcite cement	−2.6	−11.7	18.8	0.712807	0.000012
R2-21-5	3090.56	Matrix	−1.2	−6.7	24	0.709528	0.000014
		Calcite cement	−3.5	−13	17.5	0.711133	0.000016
R2-21-11	3039.13	Matrix	−0.9	−6.8	23.9	0.709042	0.000014
		Calcite cement	−7.2	−10.3	20.3	0.710392	0.000016
R2-21-21	3024	Matrix	/	/	/	0.710641	0.000014
		Calcite cement	/	/	/	0.710564	0.000018
FG3-21-3	3142.2	Matrix	0.1	−5.8	24.9	0.710531	0.000013
		Calcite cement	−7.4	−11.8	18.8	0.709961	0.000012
FG3-21-5	3141.58	Matrix	0.2	−5.2	25.6	0.70952	0.000019
		Calcite cement	−10.9	−12.3	18.2	0.710571	0.000016
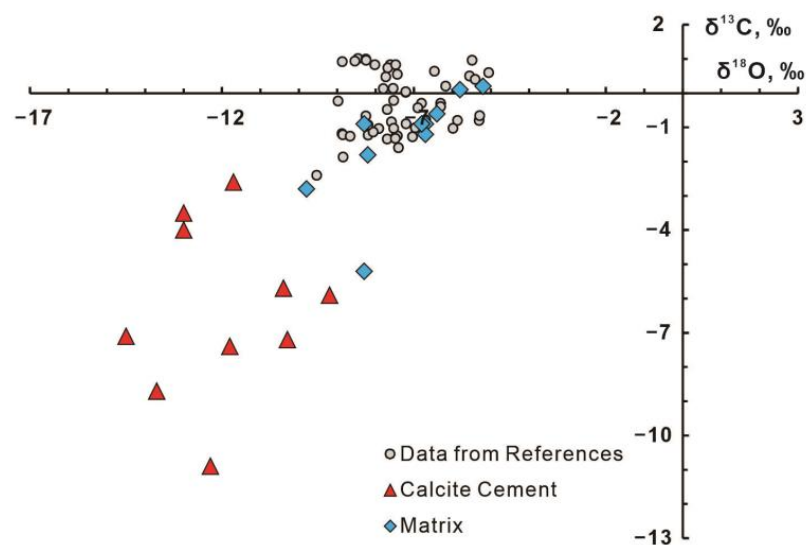
Figure 4. Carbon and oxygen isotopic characteristics of matrix and calcite cement in Majiagou Formation, Ordos Basin (C and O isotopic values of the Middle Ordovician seawater from refs. [49–51]).
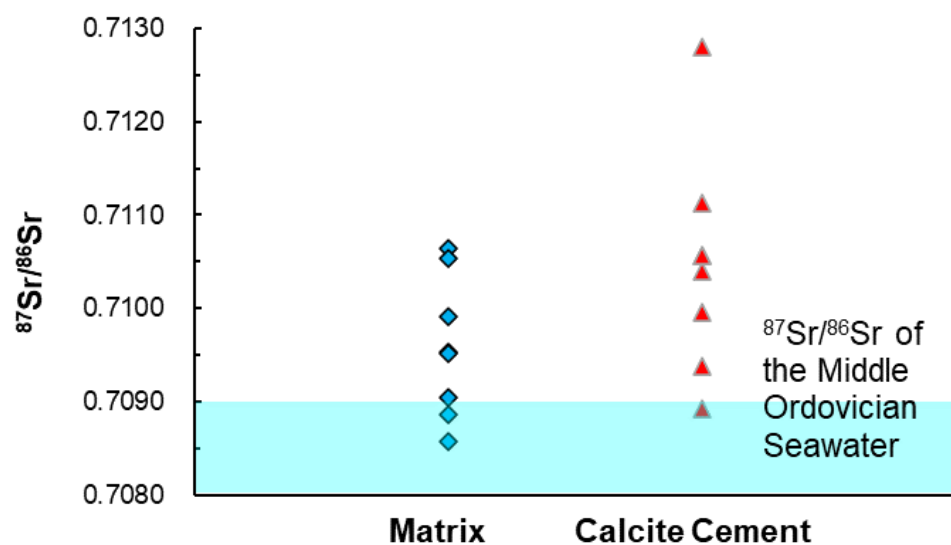
Figure 5. Strontium isotopic characteristics of matrix and calcite cement in Majiagou Formation, Ordos Basin (Sr isotope ratios of the Middle Ordovician seawater from ref. [52]).

5. Discussion

5.1. Characteristics and Origin of Cements in Karst Reservoirs

5.1.1. Evidence of Meteoric Diagenesis Transformation

Dedolomitization, the process of converting dolomite to calcite, occurs in the epigenetic environment of gypsum-bearing carbonate formations, providing additional Ca^{2+} by dissolving gypsum minerals from atmospheric freshwater to replace Mg^{2+} in dolomite [53,54]. The concave–convex contact between calcite and dolomite in the matrix is a critical feature of dedolomitization (Figure 2b), and calcite cement is a key by-product [55]. The C and O isotopes of the calcite cements also indicated a significant presence of atmospheric freshwater [13]; in addition, there was a positive correlation between them (Figure 3), and the $\delta^{18}O$ showed an obvious negative bias. Moreover, the Sr isotopic ratio values were high (Figure 4), which suggests meteoric cementation or dissolution of older rock with similar varying Sr ratios [56]. However, the cores in deeper layers did not exhibit any obvious dissolution phenomenon. The $^{87}Sr/^{86}Sr$ ratio of global runoff is 0.7119, which is similar to our obtained values [57]; therefore, the high Sr isotopic ratios strongly suggest the presence of meteoric cementation.

The homogenization temperature of fluid inclusions is a good method to detect the time of cementation [58]. A type of calcite cement filled the fractures, and the homogenization temperature of the fluid inclusions was >100 °C which much higher than the formation temperature of meteoric calcite, indicated the remaining presence of some cements during the burial period (Cal-5). The CL intensity of Cal-5 was a transition between dull red and deep red luminescent (Figure 2h), and it was difficult to distinguish from Cal-3 solely by lithological characteristics. The elemental compositions of Cal-5 had distinct characteristics that were significantly different from those of other types of cement, and the elemental concentrations were lower than those in other types of cement as well. Additionally, the REE pattern was Pattern-5 (Figure 3e). Compared with the other calcite cements, Cal-5 had unique characteristics, the lowest CI value, low Fe and Mn contents (Figure 6a–c), and monotonically decreasing REE distribution. In addition, there was no positive Eu anomaly, indicating no effects from potential abnormally high temperatures or hydrothermal fluids [59,60]. Combined the ∑REE content and CI, the Cal-5 should precipitate during the burial period was unaffected by terrigenous debris and/or late diagenesis and that the fluid source was residual pore water or pure groundwater (Figure 6d,e).
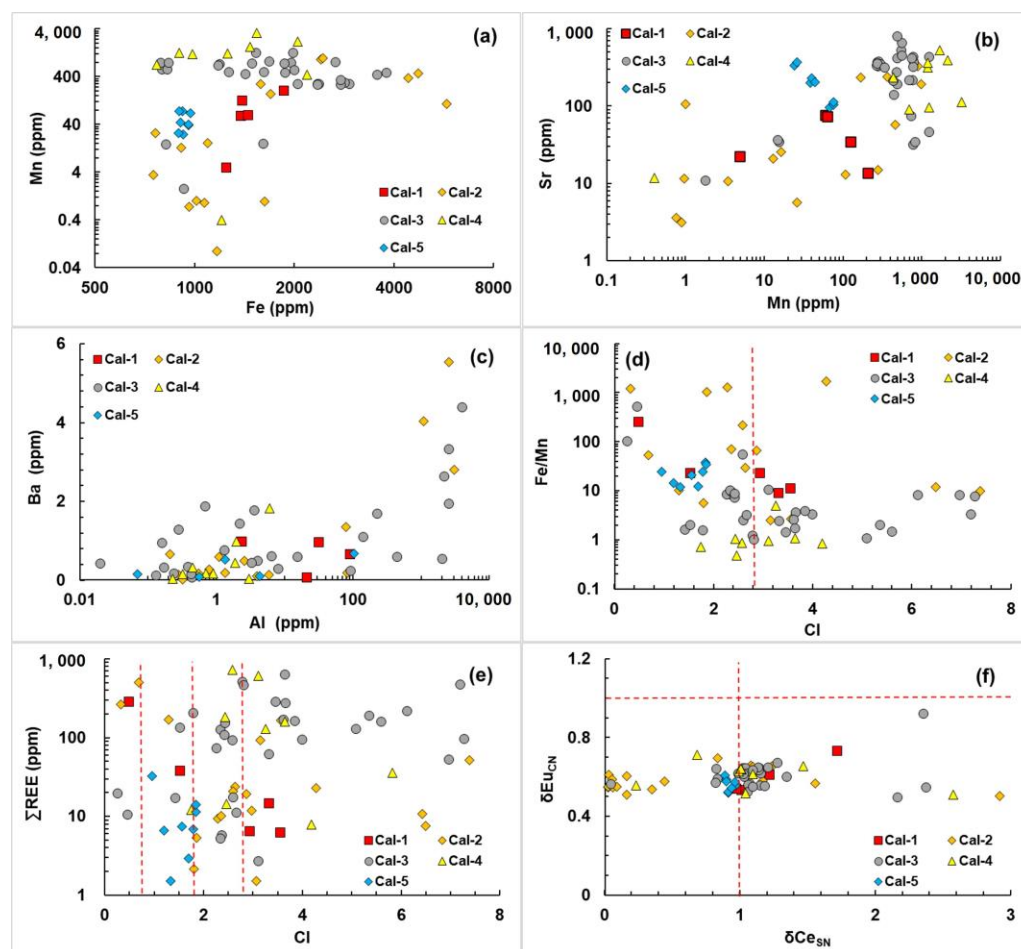
Figure 6. The in situ elemental characteristics of various cements showed regular changes in Majiagou Formation, Ordos Basin. Mn content versus (**a**) Fe, and (**b**) Sr contents, (**c**) Al versus Ba content, (**d**) Cl content versus Fe/Mn ratio, (**e**) Cl versus ∑REE contents, and (**f**) δCe_{SN} versus δEu_{CN}.

5.1.2. Characteristics of Multi-Period Meteoric Calcite Cements

The petrographic and isotopic characteristics described above indicate that four types of calcite cements were of meteoric origin. However, during a long-term weathering process, the properties of meteoric freshwater in an open system can easily be changed by factors such as weathering intensity and sea level. To further explore the origins of the calcite cements, in situ REE and major and trace elemental analysis were used to study the samples in detail [30,31].

According to the development positions and the CL intensity, four types of meteoric calcite cements were present in the study area (Figure 2). The CL intensity in the weathering crust had regular changes. The O_2 contents gradually decrease from aerobic respiration to manganese reduction in a suboxic environment, and the CL intensity changes from dull to bright red and continues to transition to dull again [61]. The CL results for Cal-1 were dull red ring-shaped calcite that was more euhedral and had a more complete crystalline form than the others (Figure 2c,d); therefore, it would have precipitated slowly during the early stage, when the pore space was the greatest. The characteristic REE pattern was Pattern-1, the ∑REE content was low, the δCe_{SN} values were generally >1.0, the CIs were ~3.0, and the δEu_{CN} values were all <1.0. REEs are an effective indicator for recovering paleoenvironments (Figure 6d–f), but they are highly susceptible to terrigenous debris and late diagenesis [62]. In general, the mixing of terrigenous detrital materials leads to a significant increase in the ∑REE content [63,64]. The lower ∑REE of Cal-1 could represent a relatively pure meteoric freshwater environment. In addition, δCe_{SN} and δEu_{CN} can be used to assess the redox status of fluid during precipitation as well as the

influence of temperature [65]. Cal-1 was formed under oxidizing conditions and were not affected by abnormal thermal events. Elemental features can effectively identify the origin of authigenic minerals: in particular, the composition and distribution pattern of REE can precisely identify the fluid source [62,66]. The characteristics of Cal-1 are a complete euhedral form; a unique ring-shaped CL luminescent; Pattern-1; moderate CI, Fe, Mn, and Ba content; and low $\sum$REE all suggest that the meteoric fluid may have been polluted by few terrigenous (Figure 6; Table 2) [40,64]. Moreover, the fluid content was low; therefore, precipitation occurred only at the pore edges and not on a large scale.

The characteristics of Cal-2 were similar to those of Cal-1, and the CL was dull luminescent. Cal-2 first developed at the pore edges or as the central fulcrum for subsequent precipitation (Figure 2d,e). The characteristic pattern of Cal-2 was Pattern-3, and most of the δCe_{SN} values were far less than 1.0 (Figure 6f). Therefore, the diagenetic fluid of Cal-2 would have been similar to that of Cal-1 except that the diagenetic fluid of Cal-2 might have been more biased toward oxidizing conditions. In addition, the REE distribution features were Pattern-3 and partial Pattern-1, and the significant negative Ce anomaly is typical characteristics of meteoric cementation. The low Fe, Mn, Ba, and Al contents, low $\sum$REE, and low CI value further demonstrate that the source was pure meteoric fluid during this period and that the pollution by terrigenous debris was low (Table 2, Figure 6).

The CL of Cal-3 was a transition luminescence that exhibited changes between dull red and deep red luminescence, and Cal-3 was more extensive than the other types of cement (Figure 2e). The highest concentrations of Fe, Sr, and Ba were present in Cal-3 and indicated a strong influence of terrigenous debris. Fe, Mn, Ba, Al, and Sr are key elements for identifying the origin of calcite [64]. Fe and Mn in carbonate mostly come from early precipitation or late metasomatism and generally enter the carbonate minerals in the form of divalent ions to replace Ca^{2+} at high temperatures and under reducing conditions [13]. However, during the epigenetic and shallow burial period, the environmental conditions are mostly low temperature and oxidizing and are not suitable for Fe^{2+} and Mn^{2+} to enter the crystal. Therefore, the Fe and Mn contents in the meteoric calcite show a wide range, indicating precipitation form a variety of fluid sources (Figure 6a,b). Owing to long-term weathering, there were clear differences in the contents of terrigenous debris, which would have been carried by different stages of fluids. Notably, Al and Ba mainly from terrigenous sources could be used to characterize the differences in the contents of terrigenous debris (Figure 6c). Cal-3 was widely distributed in the study area; its petrological characteristics were not obvious, but the characteristic REE pattern was Pattern-4 (Figure 3d), it had high $\sum$REE contents and the highest CI, and most of the δCe_{SN} values were distributed between 0.9 and 1.0 except for individual positions (Figure 6f). CI can effectively identify fluid sources. Compared with the traditional HREE/LREE versus MREE/MREE* plot [67], CI is better suited for distinguishing potential effects of seawater, pore water, and detrital signals in authigenic minerals [66]. Therefore, Cal-3 was most affected by terrigenous debris, consistent with the trends shown by $\sum$REE and other elements [66], and the environment may have been suboxic. The reason for the enrichment of MREE in Cal-3 was the enhanced solubility of meteoric fluids caused by weathering [68]. Oxidative weathering of pyrite (common near regolith), other sulfides, and/or siderite often leads to the formation of secondary iron oxides [69], whose modification of REE is focused on the depletion of LREE and on the enrichment of MREE [70].

The CL of Cal-4 was bright red luminescent, its elemental characteristics were similar to those of Cal-3, and the REE pattern was Pattern-1 (Figure 3a). Therefore, Cal-4 developed in an environment similar to that of Cal-3, which was strongly affected by terrigenous debris. Cal-4 was the last cementation to occur during the epigenetic stage. The high contents of Mn, Fe, and $\sum$REE indicate that the source was not pure, given that the REE distribution was Pattern-1 (Figure 3a), which is completely consistent with that of the matrix. Therefore, the meteoric fluid would have had strong dissolving capability. During this period, the fluid would have flowed through the matrix and strongly transformed the elemental composition; this is consistent with the observation of similar $^{87}Sr/^{86}Sr$ ratios for

the matrix and cement (Figure 5). Weathering caused an increase in the $^{87}Sr/^{86}Sr$ ratios [71], and the meteoric fluid that contained weathering information precipitated at the residual positions of the pores and/or cracks to form Cal-4 after modifying the matrix.

The origins of Cal-1 and Cal-2 were similar, and those of Cal-3 and Cal-4 were similar, which suggests that the meteoric calcites were mainly precipitated in two periods in the study area. The initial fluid was clean and was not strongly affected by terrigenous debris. However, the subsequent fluids were mixed with terrigenous debris and had strong dissolution capability. As the matrix was transformed, the REE distribution characteristics were inherited by the freshwater calcite.

5.2. Evolution Process of the Karst Reservoir Affected by Meteoric Diagenesis

The paleoenvironment is a significant factor affecting the precipitation of carbonate minerals. When the temperature increases from 5 °C to 70 °C, the precipitation rate of calcite can be increased by 3–4 times [72]. In their experiments, Burton and Walter demonstrated that for both aragonite and calcite, the precipitation rate was greatly increased at 35 °C compared with 5 °C and 17 °C [73]. The calcite cements in the study area were mainly precipitated at 319.0~292.7 Ma [22], which was at the low point of the paleotemperature of the LPIA (Figure 1a). Long-term low temperatures are not favorable for the precipitation of authigenic calcite minerals, but recent studies have determined that the LPIA was not a long-term continuous glacial action but rather was composed of glacial events separated by multiple warm events [44,74]. In the NCC, a set of basin-wide stable bauxite deposited developed during the Late Carboniferous as a result of deposition in a warm and humid climate (Figure 1c). Therefore, at 315 Ma, there would have been a long warm event in the NCC [46]; Davydov and Cózar used C and O isotope excursions to identify a period of global warming (c. 319 Ma) [45]; and a short-term climate warming (c. 304 Ma, Kasimovian period) was identified, in which atmospheric CO_2 partial pressure doubled [47].

Terrigenous debris is a major source of strontium in authigenic carbonate minerals [64]. Because the main period of calcite precipitation in the study area was during the Late Carboniferous, the NCC was within a period of uplift and denudation, and seawater had not yet re-entered the craton basin; therefore, it was difficult for seawater Sr to act as a strontium source in the precipitation of calcite cement. The Sr contents also indicated the weathering intensity and the amount of terrigenous debris, which showed similar characteristics to the contents of other elements. This phenomenon might have been caused by the influence of Benxi Formation bauxite.

Geochemical information indicated meteoric calcite cements precipitated in two periods (Figure 7), which matched with the in situ U-Pb dating reported by Zhou et al. (2022) [22]. The iron in the calcite cement mainly came from the overlying bauxite [13], so the period of Cal-1 and Cal-2 precipitation would have been earlier than that of the Moscovian bauxite and would have occurred within the warming event that occurred at c. 319 Ma. Correspondingly, the Fe and Mn contents of Cal-3 and Cal-4 were higher than in other stages. These large amounts of Fe and Mn suggest that the fluid was more contaminated by terrigenous debris than the other calcites [75], and the terrigenous debris might have originated from bauxite that was deposited simultaneously or earlier. The CL intensity showed transitions and bright red luminescence (Figure 2e), indicating that the fluid environment had changed from the strongly oxidizing conditions of the original meteoric fluid. Regarding manganese reduction, Mn^{4+} underwent a reduction reaction and became divalent before it could enter the interior of the calcite lattice [61]. A suboxic environment was favorable for a positive δCe_{SN} (Pattern-2) value and for a CL transition and bright red luminescence. The period of Cal-3 and Cal-4 precipitation would have been within the climate warming event during the Kasimovian (Figure 1c). During the Permian–Triassic, the Ordos Basin experienced multiple thermal events and the geothermal temperature of the Majiagou Fm. gradually evolved to 100 °C (Figure 7). The acidity of the formation fluid may have been weakened because of the transformation of clay minerals, resulting in the precipitation of Cal-5 (Figure 3e). However, owing to formation

fluid low content, the late calcite cement (Cal-5) precipitated during the burial period had a weaker effect on the stimulation of reservoirs and on hydrocarbon accumulation than meteoric calcite.
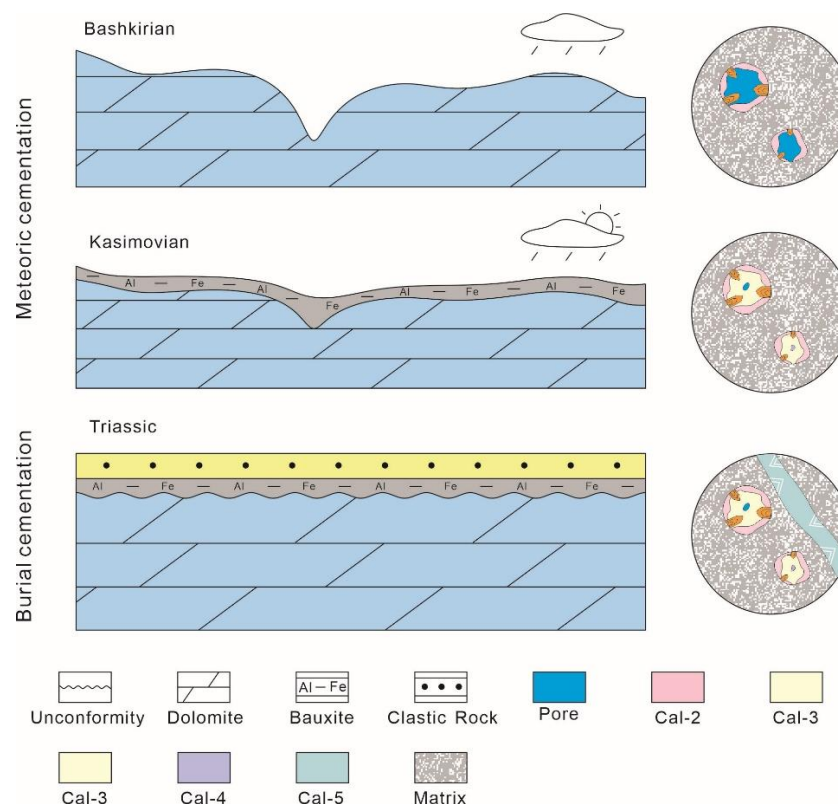

Figure 7. Burial history and diagenesis evolution of Majiagou Formation reservoirs in the Ordos Basin.

6. Conclusions

(1)   The dolomite reservoirs in the Majiagou Formation of the Ordos Basin were formed through a long-term karst process, resulting in high-quality reservoirs. However, the presence of simultaneously precipitated meteoric calcite cement (Cal-1~Cal-4) and burial cementation (Cal-5) has caused reservoir damage.

(2)   Cal-1 had a rhombohedral habit, and the REE pattern was flat. Cal-2 had dull luminescence, and had the lowest Fe, Mn, Al, and $\sum$REE contents; the REE pattern had a negative Ce anomaly. The REE pattern of Cal-3 showed MREE enrichment. Cal-4 had bright red luminescence and the highest contents of Fe, Mn, Al, and $\sum$REE. In addition, the REE pattern of Cal-5 decreased monotonically.

(3)   Cal-1 and Cal-2 formed during the Bashkirian period (*c.* 319 Ma), while Cal-3 and Cal-4 precipitated during the Kasimovian period (*c.* 304 Ma) after bauxite precipitation. These meteoric cementation events were influenced by specific geological conditions.

(4)   The cementation by meteoric calcite (Cal-1~Cal-4) occurred prior to the oil and gas charging period, causing significant damage to the karst reservoirs compared to Cal-5. Among them, Cal-3 had the most detrimental impact. Therefore, for oil and gas exploration and development in the study region, areas with higher paleogeographical locations during the critical period (Late Carboniferous) should be prioritized.

References

1. Li, Z.Q.; Goldstein, R.H.; Franseen, E.K. Climate, duration, and mineralogy controls on meteoric diagenesis, La Molata, southeast Spain. *Interpretation* **2014**, *2*, SF111–SF123. [CrossRef]
2. Csoma, A.E.; Goldstein, R.H.; Mindszenty, A.; Simone, L. Diagenetic salinity cycles and sea level along a major unconformity, Monte Composauro, Italy. *J. Sediment. Res.* **2004**, *74*, 889–903. [CrossRef]
3. Li, Z.Q.; Goldstein, R.H.; Franseen, E.K. Meteoric calcite cementation: Diagenetic response to relative fall in sea-level and effect on porosity and permeability, Las Negras area, southeastern Spain. *Sediment. Geol.* **2017**, *348*, 1–18. [CrossRef]
4. Fritz, R.D.; Wilson, J.L.; Yurewicz, D.A. Preface. In *Paleokarst Related Hydrocarbon Reservoirs*; Fritz, R.D., Wilson, J.L., Yurewicz, D.A., Eds.; SEPM: Tulsa, OK, USA, 1993.
5. Cazarin, C.L.; Bezerra, F.H.R.; Borghi, L.; Santos, R.V.; Favoreto, J.; Brod, J.A.; Auler, A.S.; Srivastava, N.K. The conduit-seal system of hypogene karst in Neoproterozoic carbonates in northeastern Brazil. *Mar. Petrol. Geol.* **2019**, *101*, 90–107. [CrossRef]
6. Ennes-Silva, R.A.; Bezerra, F.H.R.; Nogueira, F.C.C.; Balsamo, F.; Klimchouk, A.; Cazarin, C.L.; Auler, A.S. Superposed folding and associated fracturing influence hypogene karst development in Neoproterozoic carbonates, São Francisco Craton, Brazil. *Tectonophysics* **2016**, *666*, 244–259. [CrossRef]
7. Klimchouk, A.; Auler, A.S.; Bezerra, F.H.R.; Cazarin, C.L.; Balsamo, F.; Dublyansky, Y. Hypogenic origin, geologic controls and functional organization of a giant cave system in Precambrian carbonates, Brazil. *Geomorphology* **2016**, *253*, 385–405. [CrossRef]
8. Miranda, T.S.; Santos, R.F.; Barbosa, J.A.; Gomes, I.F.; Alencar, M.L.; Correia, O.J.; Falcão, T.C.; Gale, J.F.W.; Neumann, V.H. Quantifying aperture, spacing and fracture intensity in a carbonate reservoir analogue: Crato Formation, NE Brazil. *Mar. Petrol. Geol.* **2018**, *97*, 556–567. [CrossRef]
9. Bagherpour, B.; Mehrabi, H.; Faghih, A.; Vaziri-Moghaddam, H.; Omidvar, M. Tectono-eustatic controls on depositional setting and spatial facies distribution of Coniacian–Santonian sequences of the Zagros Basin in Fars area, S. Iran. *Mar. Petrol. Geol.* **2021**, *129*, 105072. [CrossRef]
10. He, Z.L.; Wei, X.C.; Qian, Y.X.; Bao, Z.Y.; Fan, M.; Jiao, C.L.; Peng, S.T.; Chen, D. Forming mechanism and distribution prediction of quality marine carbonate reservoirs (in Chinese with English abstract). *Oil Gas Geol.* **2011**, *32*, 489–498.
11. Jiang, Q.C.; Hu, S.Y.; Wang, Z.C.; Chi, Y.L.; Yang, Y.; Lu, W.H.; Wang, H.Z.; Li, Q.F. Paleokarst landform of the weathering crust of Middle Permian Maokou Formation in Sichuan Basin and selection of exploration regions. *Acta Petrol. Sin.* **2012**, *33*, 949–960. [CrossRef]
12. Zhao, W.Z.; Shen, A.J.; Pan, W.Q.; Zhang, B.M.; Qiao, Z.F.; Zheng, J.F. A research on carbonate karst reservoirs classification and its implication on hydrocarbon exploration: Case studies from Tarim Basin (in Chinese with English abstract). *Acta Petrol. Sin.* **2013**, *29*, 3213–3222.
13. Zhang, J.; He, Z.; Yu, X.; Sun, Y.; Jin, X.; Chen, X. Genesis of iron-rich dolostones in the 5th member of the Majiagou Formation of the Ordovician in Ordos Basin (in Chinese with English abstract). *Oil Gas Geol.* **2017**, *38*, 776–783. [CrossRef]
14. He, Z.L.; Ma, Y.S.; Zhu, D.Y.; Duan, T.Z.; Geng, J.H.; Zhang, J.T.; Ding, Q.; Qian, Y.X.; Wo, Y.J.; Gao, Z.Q. Theoretical and technological process and research direction of deep and ultra-deep carbonate reservoirs (in Chinese with English abstract). *Oil Gas Geol.* **2021**, *42*, 533–546. [CrossRef]
15. Xiao, D.; Cao, J.; Tan, X.; Xiong, Y.; Zhang, D.; Dong, G.; Lu, Z. Marine carbonate reservoirs formed in evaporite sequences in sedimentary basins: A review and new model of epeiric basin-scale moldic reservoirs. *Earth–Sci. Rev.* **2021**, *223*, 103860. [CrossRef]
16. Fang, S.; He, J.; Hou, F.; Yang, X.; Qiao, L.; Fu, S.; Yao, J.; Wu, Z.; Yan, R.; Xu, L. Reservoirs pore space types and evolution in M55 to M51 submembers of Majiagou Formation of Middle Ordovician in central gasfield area of Ordos basin. *Acta Petrol. Sin.* **2009**, *25*, 2425–2441.

17. He, J.; Zhao, Z.; Qiao, L.; Wei, W.; Wang, Y.; Feng, C.; Chen, B.; Chen, C. Occurrence, genesis and evolution of evaporite minerals in dolomite reservoir: A case study of the Majiagou Formation in gas fields of the central Ordos Basin (in Chinese with English abstract). *Oil Gas Geol.* **2013**, *34*, 659–666. [CrossRef]

18. Liu, X.; Zhang, D.; Dong, G.; Wang, B.; Xiao, D. Petrography and facies distribution of Middle Ordovician Ma 51+2 tight dolomite reservoirs in the Ordos Basin, Central China. *Energ. Explor. Exploit.* **2019**, *37*, 473–492. [CrossRef]

19. Fu, S.Y.; Zhang, C.G.; Chen, H.D.; Chen, A.Q.; Zhang, J.X.; Su, Z.T.; Yang, S.; Wang, G.; Mi, W.T. Characteristics, formation and evolution of pre-salt dolomite reservoirs in the fifth member of the Ordovician Majiagou Formation, mid-east Ordos Basin, NW China. *Petrol. Explor. Dev.* **2019**, *46*, 1087–1098. [CrossRef]

20. Liu, L.; Wang, C.; Du, Z.; Gong, D. Minerals Filling in Anhydrite Dissolution Pores and Their Origins in the Ordovician Majiagou Formation of the Southeastern Ordos Basin, China. *Geofluids* **2021**, *2021*, 5527299. [CrossRef]

21. Luo, Q.; Liu, B.; Shi, K.; Luo, N.; Yang, Y.; Shen, Y.; Lu, F.; Wei, L.; Wu, C.; Zhao, Q. The moldic pore evolution of the Middle Ordovician sabkha dolostone in Ordos Basin, China: A study based on the petrographic and geochemical characteristics of pore fillings. *Geol. J.* **2022**, *57*, 2812–2827. [CrossRef]

22. Zhou, J.; Yu, Z.; Wu, D.; Ren, J.; Zhang, D.; Wang, S.; Yin, C.; Liu, Y. Restoration of formation processes of dolomite reservoirs based on laser U-Pb dating: A case study of Ordovician Majiagou Formation, Ordos Basin, NW China. *Petrol. Explor. Dev.* **2022**, *49*, 327–338. [CrossRef]

23. Swart, P.K. The geochemistry of carbonate diagenesis: The past, present and future. *Sedimentology* **2015**, *62*, 1233–1304. [CrossRef]

24. Brandano, M.; Cornacchia, I.; Raffi, I.; Tomassetti, L. The Oligocene–Miocene stratigraphic evolution of the Majella carbonate platform (Central Apennines, Italy). *Sediment. Geol.* **2016**, *333*, 1–14. [CrossRef]

25. Ying, Y.; Chen, W.; Simonetti, A.; Jiang, S.; Zhao, K. Significance of hydrothermal reworking for REE mineralization associated with carbonatite: Constraints from in situ trace element and C-Sr isotope study of calcite and apatite from the Miaoya carbonatite complex (China). *Geochim. Cosmochim. Acta* **2020**, *280*, 340–359. [CrossRef]

26. Esteban, M.; Klappa, C.F. Subaerial exposure environments. In *Carbonate Depositional Environments*; Scholle, P.A., Bebout, D.G., Moore, C.H., Eds.; American Association of Petroleum Geologists: Tulsa, OK, USA, 1983. [CrossRef]

27. Andrews, J.E.; Pedley, H.M.; Dennis, P.F. Stable isotopic record of palaeoclimatic change in a British Holocene tufa. *Holocene* **1994**, *4*, 349–355. [CrossRef]

28. Muchez, P.; Nielsen, P.; Sintubin, M.; Lagrou, D. Conditions of meteoric calcite formation along a Variscan fault and their possible relation to climatic evolution during the Jurassic–Cretaceous. *Sedimentology* **1998**, *45*, 845–854. [CrossRef]

29. Defliese, W.; Lohmann, K. Evaluation of meteoric calcite cements as a proxy material for mass-47 clumped isotope thermometry. *Geochim. Cosmochim. Acta* **2016**, *173*, 126–141. [CrossRef]

30. Webb, G.; Nothdurft, L.D.; Kamber, B.S.; Kloprogge, J.T.; Zhao, J. Rare earth element geochemistry of scleractinian coral skeleton during meteoric diagenesis: A sequence through neomorphism of aragonite to calcite. *Sedimentology* **2009**, *56*, 1433–1463. [CrossRef]

31. Himmler, T.; Bach, W.; Bohrmann, G.; Peckmann, J. Rare earth elements in authigenic methane-seep carbonates as tracers for fluid composition during early diagenesis. *Chem. Geol.* **2010**, *277*, 126–136. [CrossRef]

32. Barnaby, R.J.; Rimstidt, J.D. Redox conditions of calcite cementation interpreted from Mn and Fe contents of authigenic calcites. *Geol. Soc. Am. Bull.* **1989**, *101*, 795–804. [CrossRef]

33. Wei, D.; Gao, Z.; Fan, T.; Niu, Y.; Guo, R. Volcanic events-related hydrothermal dolomitisation and silicification controlled by intra-cratonic strike-slip fault systems: Insights from the northern slope of the Tazhong Uplift, Tarim Basin, China. *Basin Res.* **2021**, *33*, 2411–2434. [CrossRef]

34. Huang, B.; Yan, Y.; Piper, J.D.A.; Zhang, D.; Yi, Z.; Yu, S.; Zhou, T. Paleomagnetic constraints on the paleogeography of the East Asian blocks during Upper Paleozoic and Lower Mesozoic times. *Earth Sci. Rev.* **2018**, *186*, 8–36. [CrossRef]

35. Trotter, J.; Williams, I.; Barnes, C.; Lecuyer, C.; Nicoll, R. Did Cooling Oceans Trigger Ordovician Biodiversification? Evidence From Conodont Thermometry. *Science* **2008**, *321*, 550–554. [CrossRef] [PubMed]

36. Wang, B.; Al-Aasm, I. Karst-controlled diagenesis and reservoir development: Example from the Ordovician main-reservoir carbonate rocks on the eastern margin of the Ordos basin, China. *AAPG Bull.* **2002**, *86*, 1639–1658. [CrossRef]

37. Yang, P.; Ren, Z.; Zhou, R.; Cui, J.; Qi, K.; Fu, J.; Li, J.; Liu, X.; Li, W.; Wang, K. Tectonic evolution and controls on natural gas generation and accumulation in the Ordovician system of the Ordos Basin, North China. *Energy Rep.* **2021**, *7*, 6887–6898. [CrossRef]

38. Yang, Y.; Li, W.; Ma, L. Tectonic and stratigraphic controls of hydrocarbon systems in the Ordos basin: A multicycle cratonic basin in central China. *AAPG Bull.* **2005**, *89*, 255–269. [CrossRef]

39. Yu, Z.; Yu, Z.C.; Wu, D.X.; Dong, Y.; Guo, T.; Liu, W. Sedimentary facies evolution model of Ordovician Majiagou Foramtion, Central-Eastern Ordos Basin (in Chinese with English abstract). *Marin. Orig. Petrl. Geol.* **2017**, *22*, 12–22. [CrossRef]

40. Yang, J.Q.; Zhang, J.T.; He, Z.L.; Luo, N.N.; Jin, X.H.; Zhang, T.; Gu, N.; Huang, K.J.; Gao, J. Fractionation characteristics of magnesium isotope in the ancient weathering crust. *Petrol. Sci.* **2022**, *in press*. [CrossRef]

41. Xiong, Y.; Hou, Z.M.; Tan, X.C.; Luo, J.S.; Yue, Y.; Wu, K.Y. Constraining fluid-rock interactions during eogenetic karst and their impacts on carbonate reservoirs: Insights from reactive transport modeling. *Appl. Geochem.* **2021**, *131*, 105050. [CrossRef]

42. Saltzman, M. Late Paleozoic ice age: Oceanic gateway or pCO$_2$? *Geology* **2003**, *31*, 151–154. [CrossRef]

43. Isbell, J.; Henry, L.; Gulbranson, E.; Limarino, C.; Fraiser, M.; Koch, Z.; Ciccioli, P.; Dineen, A. Glacial paradoxes during the late Paleozoic ice age: Evaluating the equilibrium line altitude as a control on glaciation. *Gondwana Res.* **2012**, *22*, 1–19. [CrossRef]

44. Fielding, C.; Frank, T.; Birgenheier, L.; Rygel, M.; Jones, A.; Roberts, J. Stratigraphic imprint of the late Paleozoic ice age in eastern Australia: A record of alternating glacial and nonglacial climate regime. *J. Geol. Soc. Lond.* **2008**, *165*, 129–140. [CrossRef]

45. Davydov, V.; Cózar, P. The formation of the Alleghenian Isthmus triggered the Bashkirian glaciation: Constraints from warm-water benthic foraminifera. *Palaeogeogr. Palaeoclimatol. Palaeoecol.* **2019**, *531*, 108403. [CrossRef]

46. Cao, G.; Du, X. *Formation Mechanism of the Aluminiferous Rock Series in Benxi Formation, North China Block*; Science Press: Beijing, China, 2020; pp. 16–27.

47. Chen, J.; Montanez, I.; Zhang, S.; Isson, T.; Macarewich, S.; Planavsky, N.; Zhang, F.; Rauzi, S.; Daviau, K.; Yao, L.; et al. Marine anoxia linked to abrupt global warming during Earth's penultimate icehouse. *Proc. Natl. Acad. Sci. USA* **2022**, *119*, e2115231119. [CrossRef] [PubMed]

48. Rieger, P.; Magnall, J.; Gleeson, S.; Oelze, M.; Wilke, F.; Lilly, R. Differentiating between hydrothermal and diagenetic carbonate using rare earth element and yttrium (REE+Y) geochemistry: A case study from the Paleoproterozoic George Fisher massive sulfide Zn deposit, Mount Isa, Australia. *Miner. Depos.* **2022**, *57*, 187–206. [CrossRef]

49. He, X.Y.; Shou, J.F.; Shen, A.J.; Wu, X.N.; Wang, Y.S.; Hu, Y.Y.; Zhu, Y.; Wei, D.X. Geochemical characteristics and origin of dolomite: A case study from the middle assemblage of Ordovician Majiagou Formation Member 5 of the west of Jingbian Gas Field, Ordos Basin, North China. *Petrol. Explor. Dev.* **2014**, *41*, 417–427. [CrossRef]

50. Cao, H.X.; Shang, T.; Wu, H.Y.; Wang, N.X.; Feng, Y. Characteristics of carbon and oxygen isotopes of carbonate rocks in Majiagou Formation and their implication, southeastern Ordos Basin (in English abstract). *J. Northwest Univ. (Nat. Sci. Ed.)* **2018**, *48*, 578–586. [CrossRef]

51. He, M.; Huang, W.H.; Jiu, B. Origin and evolution of gypsum dolomite as a favorable reservoir in the Ordos Basin, China (in English abstract). *Earth Sci. Front.* **2021**, *28*, 327–336. [CrossRef]

52. McArthur, J.M.; Howarth, R.J.; Bailey, T.R. Strontium isotope stratigraphy: LOWESS Version 3: Best fit to the marine Sr isotope curve for 0–509 Ma and accompanying look-up table for deriving numerical age. *J. Geol.* **2001**, *109*, 155–170. [CrossRef]

53. Nader, F.H.; Swennen, R.; Keppens, E. Calcitization/dedolomitization of Jurassic dolostones (Lebanon): Results from petrographic and sequential geochemical analyses. *Sedimentology* **2008**, *55*, 1467–1485. [CrossRef]

54. Escorcia, L.C.; Gomez-Rivas, E.; Daniele, L.; Corbella, M. Dedolomitization and reservoir quality: Insights from reactive transport modelling. *Geofluids* **2013**, *13*, 221–231. [CrossRef]

55. Schoenherr, J.; Reuning, L.; Hallenberger, M.; Lüders, V.; Lemmens, L.; Biehl, B.; Lewin, A.; Leupold, M.; Wimmers, K.; Strohmenger, C. Dedolomitization: Review and case study of uncommon mesogenetic formation conditions. *Earth Sci. Rev.* **2018**, *185*, 780–805. [CrossRef]

56. Gao, J.; He, S.; Zhao, J.; He, Z.; Wu, C.; Feng, Y.; Nguyen, A.; Zhou, J.; Yi, Z. Sm-Nd isochron dating and geochemical (rare earth elements, $^{87}Sr/^{86}Sr$, $\delta^{18}O$, $\delta^{13}C$) characterization of calcite veins in the Jiaoshiba shale gas field, China: Implications for the mechanisms of vein formation in shale gas systems. *Geol. Soc. Am. Bull.* **2020**, *132*, 1722–1740. [CrossRef]

57. Palmer, M.R.; Edmond, J.M. The strontium isotope budget of the modern ocean. *Earth Planet. Sc. Lett.* **1989**, *92*, 11–26. [CrossRef]

58. Yang, T.; Azmy, K.; He, Z.; Li, S.; Liu, E.; Wu, S.; Wang, J.; Li, T.; Gao, J. Fault-controlled hydrothermal dolomitization of Middle Permian in southeastern Sichuan Basin, SW China, and its temporal relationship with the Emeishan Large Igneous Province: New insights from multi-geochemical proxies and carbonate U–Pb dating. *Sediment. Geol.* **2022**, *439*, 106215. [CrossRef]

59. Ren, Z.; Zhang, S.; Gao, S.; Cui, J.; Xiao, Y.; Xiao, H. Tectonic thermal history and its significance on the formation of oil and gas accumulation and mineral deposit in Ordos Basin. *Sci. China Earth Sci.* **2007**, *50*, 27–38. [CrossRef]

60. Jiu, B.; Huang, W.; Li, Y. The effect of hydrothermal fluids on Ordovician carbonate rocks, southern Ordos Basin, China. *Ore Geol. Rev.* **2020**, *126*, 103803. [CrossRef]

61. Petrash, D.; Bialik, O.; Staudigel, P.; Konhauser, K.; Budd, D. Biogeochemical reappraisal of the freshwater–seawater mixing-zone diagenetic model. *Sedimentology* **2021**, *68*, 1797–1830. [CrossRef]

62. Mishra, P.; Mohanty, S. Geochemistry of carbonate rocks of the Chilpi Group, Bastar Craton, India: Implications on ocean paleoredox conditions at the late Paleoproterozoic Era. *Precambrian Res.* **2021**, *353*, 106023. [CrossRef]

63. Yang, J.Q.; Zhang, J.T.; He, Z.L.; Zhang, T. Paleoenvironment reconstruction of the Middle Ordovician thick carbonate from western Ordos Basin, China. *Petrol. Sci.* **2023**, *20*, 48–59. [CrossRef]

64. Zhang, P.; Wang, Y.; Zhang, X.; Wei, Z.; Wang, G.; Zhang, T.; Ma, H.; Wei, J.; He, W.; Ma, X.; et al. Carbon, oxygen and strontium isotopic and elemental characteristics of the Cambrian Longwangmiao Formation in South China: Paleoenvironmental significance and implications for carbon isotope excursions. *Gondwana Res.* **2022**, *106*, 174–190. [CrossRef]

65. Bau, M.; Möller, P. Rare earth element fractionation in metamorphogenic hydrothermal calcite, magnesite and siderite. *Miner. Petrol.* **1992**, *45*, 231–246. [CrossRef]

66. Bayon, G.; Lambert, T.; Vigier, N.; Deckker, P.; Freslon, N.; Jang, K.; Larkin, C.; Piotrowski, A.; Tachikawa, K.; Thollon, M.; et al. Rare earth element and neodymium isotope tracing of sedimentary rock weathering. *Chem. Geol.* **2020**, *553*, 119794. [CrossRef]

67. Du, J.; Haley, B.A.; Mix, A.C. Neodymium isotopes in authigenic phases, bottom waters and detrital sediments in the Gulf of Alaska and their implications for paleocirculation reconstruction. *Geochim. Cosmochim. Acta* **2016**, *193*, 14–35. [CrossRef]

68. Blattmann, T.M.; Wang, S.L.; Lupker, M.; Märki, L.; Haghipour, N.; Wacker, L.; Chung, L.-H.; Bernasconi, S.M.; Plötze, M.; Eglinton, T.I. Sulphuric acid-mediated weathering on Taiwan buffers geological atmospheric carbon sinks. *Sci. Rep.* **2019**, *9*, 2945. [CrossRef] [PubMed]

69. Lara, R.H.; Monroy, M.G.; Mallet, M.; Dossot, M.; González, M.A.; Cruz, R. An experimental study of iron sulfides weathering under simulated calcareous soil conditions. *Environ. Earth Sci.* **2015**, *73*, 1849–1869. [CrossRef]

70. Franchi, F.; Rovere, M.; Gamberi, F.; Rashed, H.; Vaselli, O.; Tassi, F. Authigenic minerals from the Paola Ridge (southern Tyrrhenian Sea): Evidences of episodic methane seepage. *Mar. Petrol. Geol.* **2017**, *86*, 228–247. [CrossRef]

71. Cornacchia, I.; Brandano, M.; Agostini, S. Miocene paleoceanographic evolution of the Mediterranean area and carbonate production changes: A review. *Earth Sci. Rev.* **2021**, *221*, 103785. [CrossRef]

72. Lopez, O.; Zuddas, P.; Faivre, D. The influence of temperature and seawater composition on calcite crystal growth mechanisms and kinetics: Implications for Mg incorporation in calcite lattice. *Geochim. Cosmochim. Acta* **2009**, *73*, 337–347. [CrossRef]

73. Burton, E.; Walter, L. Relative precipitation rates of aragonite and Mg calcite from seawater: Temperature or carbonate ion control? *Geology* **1987**, *15*, 111–114. [CrossRef]

74. Gulbranson, E.; Montanez, I.; Schmitz, M.; Limarino, C.; Isbell, J.; Marenssi, S.; Crowley, J. High-precision U-Pb calibration of Carboniferous glaciation and climate history, Paganzo Group, NW Argentina. *Geol. Soc. Am. Bull.* **2010**, *122*, 1480–1498. [CrossRef]

75. Feng, Y.; Xiao, X.M.; Gao, P.; Wang, E.Z.; Hu, D.F.; Liu, R.B.; Li, G.; Lu, C.G. Restoration of sedimentary environment and geochemical features of deep marine Longmaxi shale and its significance for shale gas: A case study of the Dingshan area in the Sichuan Basin, South China. *Mar. Pet. Geol.* **2023**, *151*, 106186. [CrossRef]